Target positioning for active sonar based on 1-bit gridless compressed sensing

GAO Yiding[1,2] WU Min[1,2†] HAO Chengpeng[1,2,3†] WU Yongqing[1,2] LIU Luoran[1,2]

1 Institute of Acoustics, Chinese Academy of Sciences, Beijing 100190, China
2 University of Chinese Academy of Sciences, Beijing 100049, China
3 State Key Laboratory of Acoustics and Marine Information, Beijing 100190, China

Received December 19, 2025; accepted January 31, 2026

Abstract To enable precise target positioning in constrained underwater platforms with limited storage, we propose a 1-bit quantized frequency diverse array multiple-input multiple-output (FDA-MIMO) sonar system. The FDA-MIMO sonar significantly enhances target localization by providing both range and angular resolution. However, the coupling between range and angle in traditional FDA-MIMO processing leads to parameter estimation ambiguity, and grid-based compressed sensing (CS) methods suffer from grid mismatch, resulting in reduced accuracy. To overcome these challenges, we present a 1-bit gridless CS-based target positioning algorithm for accurate underwater localization. First, we develop an array expansion model to decouple the range and angle parameters. Then, leveraging gridless CS with 1-bit quantization, we reformulate the joint estimation as an atomic norm minimization problem. Using convex relaxation, we convert this into an asymmetric cone programming problem and propose an efficient, fast interior-point method for rapid optimization. Numerical simulations show that the proposed algorithm excels in both estimation accuracy and computational speed.

Keywords FDA-MIMO sonar, 1-bit quantization, Compressed sensing, Joint range-angle estimation, Fast interior-point method

PACS: 43.30, 43.60 **DOI:** 10.3724/0217-9776.3025013 **CSTR:** 32050.14.11-2066.3025013

1 Introduction

In recent years, frequency diverse array multiple-input multiple-output (FDA-MIMO) sonar has attracted increasing attention due to its ability to provide additional range information on top of accurate azimuth estimation for underwater target localization. This feature enables the system to effectively resolve potential interfering targets located in the same angle bin but different range bins, thereby enhancing the robustness of underwater localization systems[1,2]. Consequently, various two-dimensional (2D) high-resolution parameter estimation techniques, such as 2D multiple signal classification (2D-MUSIC)[3] and 2D estimation of signal parameters via rotational invariance techniques (2D-ESPRIT)[4], have been incorporated into FDA-MIMO processing frameworks. However, subspace-based methods typically require a sufficient number of independent snapshots and often fail in scenarios with highly correlated or coherent targets.

Furthermore, most target localization systems rely on high-resolution analog-to-digital converters (ADCs), which are costly and power-consuming[5], posing challenges for compact underwater platforms with limited computational and storage resources. Consequently, target localization methods based on 1-bit quantized measurements[6-8] have emerged as cost-efficient and energy-efficient alternatives suitable for resource-constrained sensing platforms.

In this work, we derive the signal model for FDA-MIMO sonar target localization and show that, under conventional FDA-MIMO processing, the inherent range-angle coupling in the transmit steering matrix may lead to ambiguity problems[2], thereby degrading the estimation performance. To address this issue, we propose an aperture-expanded model by reorganizing the received data, which effectively decouples the range and angle parameters while enlarging the virtual array aperture. Although this model improves the theoretical estimation resolution, it inevitably introduces a substantial number of missing virtual elements, causing the

This work was supported by the National Natural Science Foundation of China (62371446, 62471463) and the Youth Innovation Promotion Association, CAS (2023030).
† Corresponding author: WU Min, wumin880902@hotmail.com; HAO Chengpeng, haochengp@mail.ioa.ac.cn

© The Author(s) 2026. This is an open access article under the CC-BY 4.0 License (https://creativecommons.org/licenses/by/4.0/).

performance of conventional covariance-based beamforming and subspace methods to deteriorate significantly.

Compressed sensing (CS) theory[9] enables sparse signal recovery and frequency estimation under sub-Nyquist sampling, offering a promising solution for parameter estimation with missing data. In particular, gridless CS[10-12] extends traditional CS to the continuous domain, effectively eliminating grid mismatch and further improving estimation accuracy. For conventional linear frequency-modulated (LFM) sonar systems, a decoupled atomic norm minimization (DANM) approach was proposed in Ref. [13], which enables accurate and efficient extraction of target range and angle information. Moreover, under 1-bit quantization, a 1-bit reweighted atomic norm minimization (1-bit-RANM) method was developed in Ref. [14] to achieve higher-precision direction-of-arrival estimation.

Motivated by these observations, we develop a target positioning algorithm for active sonar based on 1-bit gridless CS. First, an aperture-expansion strategy is introduced to decouple the range and angle parameters. Then, by employing gridless CS under 1-bit quantization, the joint estimation problem is formulated as an ANM problem. Through convex relaxation, the problem is recast as an asymmetric cone program, for which we design an efficient fast interior-point method (FIPM) to enable rapid numerical computation.

The main contributions of this work are summarized as follows.

(1) Motivated by the large data volume and intensive data transmission requirements inherent in FDA-MIMO active sonar systems, this paper introduces a quantization model and a 1-bit gridless CS framework into the joint range-angle estimation problem for FDA-MIMO active sonar, thereby significantly reducing the system's data acquisition and processing burden.

(2) A virtual array expansion model is proposed for FDA-MIMO sonar, which explicitly achieves range-angle decoupling. Furthermore, to address the virtual array "hole" problem induced by array expansion, a quantization-aware atomic norm minimization formulation tailored for 1-bit measurements is developed.

(3) By exploiting the underlying problem structure, an efficient 1-bit-2D FIPM (1-bit-2D-FIPM) is designed, which substantially reduces computational complexity and accelerates convergence.

2 Signal model

An FDA-MIMO sonar system was considered, as illustrated in Fig. 1. Both the transmitting and receiving arrays are configured as uniform linear arrays (ULAs). The transmitting array consists of M elements with an inter-element spacing of d_{t}, while the receiving array comprises N elements spaced d_{r} apart. The center frequency of the transmitted signal by the mth element ($m = 0, \ldots, M-1$) is

$$f_{\mathrm{c}_m} = f_{\mathrm{c}_0} + m\Delta f, \tag{1}$$

where f_{c_0} denotes the reference frequency, and Δf is the frequency increment ensuring orthogonality between the transmitted signals. The signal transmitted by the mth element of the transmitter is

$$\mathrm{ST}_m(t) = \varphi_m(t)\exp\left\{\mathrm{j}2\pi f_{\mathrm{c}_m} t\right\},\ 0 \leqslant t \leqslant T_{\mathrm{p}}, \tag{2}$$

where T_{p} is the pulse duration, and $\varphi_m(t)\,(m = 0, 1, \cdots, M-1)$ denotes the narrowband envelope of the transmitted signal satisfying orthogonality:

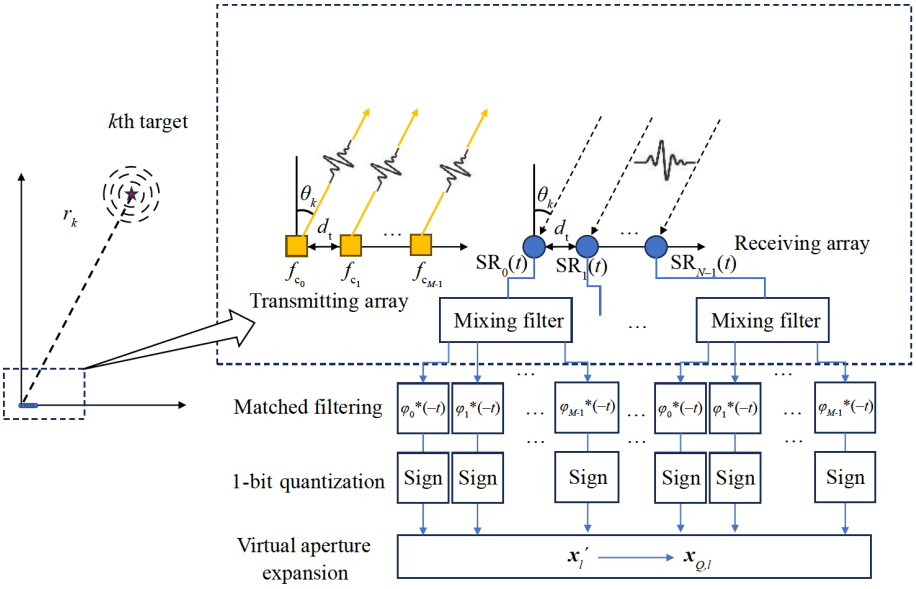


Fig. 1 Echo signal model and processing flow of an FDA-MIMO sonar system.

$$\int_0^{T_p} \varphi_{m_1}(t)\varphi_{m_2}^*(t-\tau)\mathrm{d}t = 0,\ m_1 \neq m_2,\ \forall \tau, \tag{3}$$

where τ denotes the time delay.

Using the signal received at the first element of the receiving array as the reference, we consider K far-field targets with ranges r_k and angles $\theta_k (k = 1, \cdots, K)$. As shown in Fig. 1, the propagation time delay for the signal transmitted by the mth transmitting array element, reflected by the kth target, and received by the nth receiving array element is[3]

$$\tau_{m,k,n} = \frac{2r_k - md_t\sin\theta_k - nd_r\sin\theta_k}{c}, \tag{4}$$

where c is the sound speed in water. The received signal at the nth receiving array element associated with the lth pulse echo is

$$\begin{aligned}\mathrm{SR}_{n,l}(t) = &\sum_{k=1}^{K}\sigma_{k,l}\sum_{m=0}^{M-1}\varphi(t-\tau_{m,k,n})\\ &\cdot\exp\left\{\mathrm{j}2\pi f_{\mathrm{c}_m}(t-\tau_{m,k,n})\right\},\end{aligned} \tag{5}$$

where $n = 0, \cdots, N-1$, $\sigma_{k,l}$ is the scattering coefficient of the kth target for the lth pulse.

After approximation and recombination of the received signals with matched filters, the matched filtering output for the mth reference function $\varphi_m(t)\exp\{\mathrm{j}2\pi m\Delta f t\}$ at the nth receiving element for the lth pulse is (assume $d_t / d_r = C$ is an integer)

$$\begin{aligned}x_{n,m,l} &= \sum_{k=1}^{K} s_{k,l}\exp\left\{\mathrm{j}2\pi n\frac{d_r\sin\theta_k}{\lambda_{\mathrm{wave},0}}\right\}\\ &\quad\cdot\exp\left\{\mathrm{j}2\pi m\left(\frac{d_t\sin\theta_k}{\lambda_{\mathrm{wave},0}} - \frac{2\Delta f r_k}{c}\right)\right\}\\ &= \sum_{k=1}^{K} s_{k,l}\exp\left\{\mathrm{j}2\pi\frac{d_r\sin\theta_k}{\lambda_{\mathrm{wave},0}}(Cm+n)\right\}\\ &\quad\cdot\exp\left\{\mathrm{j}2\pi\frac{2\Delta f r_k}{c}m\right\}.\end{aligned} \tag{6}$$

Equation (6) is arranged in the order of $m = 1, \cdots, M-1$ and $n = 1, \cdots, N-1$, and can be organized as

$$\begin{aligned}\mathbf{x}'_l &= \sum_{k=1}^{K} s_{k,l}\mathbf{a}_r(\theta_k)\otimes(\mathbf{b}_t(\theta_k)\odot\mathbf{c}_t(r_k))\\ &= \sum_{k=1}^{K} s_{k,l}\mathbf{a}_r(\theta_k)\otimes\mathbf{a}_t(\theta_k, r_k) \in \mathbb{C}^{MN},\end{aligned} \tag{7}$$

where $\otimes$ and $\odot$ denote the Kronecker product and Hadamard product, respectively, $\mathbf{a}_r(\theta_k) = \left[1, \exp\left\{\mathrm{j}2\pi d_r\sin\theta_k / \lambda_{\mathrm{wave},0}\right\}, \cdots, \exp\left\{\mathrm{j}2\pi d_r\sin\theta_k(N-1)/\lambda_{\mathrm{wave},0}\right\}\right]^{\mathrm{T}}$ is the steering vector of receiving array, and $\mathbf{a}_t(\theta_k, r_k) = \mathbf{b}_t(\theta_k)\odot\mathbf{c}_t(r_k)$ is the steering vector of transmitting array. $\mathbf{b}_t(\theta_k) = \left[1, \exp\left\{\mathrm{j}2\pi d_r\sin\theta_k C / \lambda_{\mathrm{wave},0}\right\}, \cdots, \exp\left\{\mathrm{j}2\pi d_r\sin\theta_k C(M-1)/\lambda_{\mathrm{wave},0}\right\}\right]^{\mathrm{T}}$ is the part about angle of $\mathbf{a}_t(\theta_k, r_k)$, $\mathbf{c}_t(r_k) = \left[1, \exp\left\{\mathrm{j}2\pi 2\Delta f r_k / c\right\}, \cdots, \exp\left\{\mathrm{j}2\pi 2\Delta f r_k(M-1)/c\right\}\right]^{\mathrm{T}}$ is the part about range of $\mathbf{a}_t(\theta_k, r_k)$. After 1-bit quantization, the observed signal is transformed into a sign-only representation:

$$\mathbf{x}'_{\mathcal{Q},l} = \mathcal{Q}\left\{\mathbf{x}'_l\right\} = \mathrm{sign}\left(\Re\left\{\mathbf{x}'_l\right\}\right) + \mathrm{j}\cdot\mathrm{sign}\left(\Im\left\{\mathbf{x}'_l\right\}\right), \tag{8}$$

where $\Re\{\cdot\}$ and $\Im\{\cdot\}$ represent the real and imaginary parts of the complex number, the operator $\mathcal{Q}\{\cdot\}$ denotes element-wise complex quantization, and the sign function is

$$\mathrm{sign}(x) = \begin{cases}1, & \text{if } x \geqslant 0,\\ -1, & \text{if } x < 0.\end{cases} \tag{9}$$

Specifically, the adopted 1-bit quantization process assumes that the received signals undergo automatic gain control prior to quantization, thereby ensuring that the sign information remains statistically meaningful. Although this simplified model does not explicitly account for non-ideal effects in the receiver chain, it has been widely used in low-bit array signal processing studies to characterize performance limits and algorithmic robustness[6-8]. In this work, the 1-bit quantization model serves as a representative abstraction for extremely low-resolution sensing scenarios, with the goal of enhancing estimation performance through the joint design of FDA-MIMO sonar configurations and quantization-aware signal processing methods.

3 The gridless joint range-angle estimation algorithm

3.1 ANM based on aperture-expansion strategy

Define $\mathbf{b}'_t(\theta_k) = \left[1, \exp\left\{\mathrm{j}2\pi d_r\sin\theta_k / \lambda_{\mathrm{wave},0}\right\}, \cdots, \exp\left\{\mathrm{j}\cdot 2\pi d_r\sin\theta_k C(M-1)/\lambda_{\mathrm{wave},0}\right\}\right]^{\mathrm{T}} \in \mathbb{C}^{CM-C+1}$ as the steering vector of array expansion about angle, and

$$\mathbf{f}(\theta_k) = \left[1, \exp\left(\mathrm{j}2\pi\frac{d_r\sin\theta_k}{\lambda_{\mathrm{wave},0}}\right), \cdots, \exp\left(\mathrm{j}2\pi\frac{d_r\sin\theta_k}{\lambda_{\mathrm{wave},0}}(C(M-1)+N-1)\right)\right] \in \mathbb{C}^{N'}, \tag{10}$$

is formed by extracting the non-redundant $N' = CM - C + N$ elements of the steering vector of array expansion $\mathbf{a}_r(\theta_k)\otimes\mathbf{b}'_t(\theta_k)$.

Then, the received quantized data is

$$\mathbf{x}_{\mathcal{Q},l'} = \mathbf{P}\mathcal{Q}\{\mathbf{x}_l\} \Leftrightarrow \mathbf{x}'_l = \mathbf{P}\mathbf{x}_l, \tag{11}$$

where

$$\mathbf{x}_l = \sum_{k=1}^{K} s_{k,l}\mathbf{f}(\theta_k) \otimes \mathbf{c}_{\mathrm{t}}(r_k) \in \mathbb{C}^{MN'}, \tag{12}$$

and $\mathbf{P} \in \mathbb{C}^{MN \times MN'}$ acts as the observation matrix mapping $\mathbf{x}_l$ to $\mathbf{x}'_l$, given by

$$\mathbf{P} = \begin{bmatrix} \mathbf{P}_1 \\ \mathbf{P}_2 \\ \vdots \\ \mathbf{P}_N \end{bmatrix}, \tag{13}$$

where $\mathbf{P}_i \in \mathbb{C}^{M \times MN'}$, $i = 1, \ldots, N$.

The jth column of $\mathbf{P}_i$ contains a single one at index:

$$1 + (i-1)M + (CM+1)(j-1), \tag{14}$$

and zeros elsewhere, for $j = 1, \ldots, M$. The aperture-expansion strategy in Eq. (12) further achieves explicit range-angle decoupling through

$$\mathbf{a}_{\mathrm{r}}(\theta_k) \otimes \mathbf{a}_{\mathrm{t}}(\theta_k, r_k) \in \mathbb{C}^{MN} \rightarrow \mathbf{f}(\theta_k) \otimes \mathbf{c}_{\mathrm{t}}(r_k) \in \mathbb{C}^{MN'}. \tag{15}$$

The 2D super-resolution[10,15,16] aims to recover continuous-domain spectral components from under-sampled samples by exploiting sparsity, eliminating the grid mismatch inherent in grid-based CS approaches.

Furthermore, the quantized measurements $\mathbf{x}'_{\mathcal{Q},l}$ can be viewed as 1-bit sampled partial observations of the full signal $\mathbf{x}_l$, while recovering $\mathbf{x}_l$ from $\mathbf{x}'_{\mathcal{Q},l}$ corresponds to a 1-bit quantized virtual-array expansion or, equivalently, sparse recovery from under-sampled data.

In our model, the vector

$$\mathbf{u} = \Big[\underbrace{u_{0,0}, u_{1,0}, \ldots, u_{M-1,0}}_{M}, \underbrace{u_{-M+1,1}, \ldots, u_{M-1,1}}_{2M-1}, \ldots, \underbrace{u_{-M+1,N'-1}, \ldots, u_{M-1,N'-1}}_{2M-1}\Big]^{\mathrm{T}} \in \mathbb{C}^{N_{\mathbf{u}}},$$
$$\mathbf{n} = [n_1, n_2]^{\mathrm{T}} \in \mathbb{N}_{\mathbf{u}} \triangleq \left\{\mathbf{n} : \begin{cases} n_1 = 0, \ldots, M-1, & \text{when } n_2 = 0, \\ n_1 = -M+1, \ldots, M-1, & \text{when } n_2 = 1, \ldots, N'-1 \end{cases}\right\}. \tag{19}$$

The positive semidefinite (PSD) constraint in Eq. (17) implicitly restricts $\mathbf{u}$ to the cone:

$$\mathcal{C} \triangleq \left\{\mathbf{u} : \mathbf{T}_{\mathrm{ML}}(\mathbf{u}) \succeq 0\right\}.$$

For any $\mathbf{u} \in \mathcal{C}$ such that $\mathrm{rank}(\mathbf{T}_{\mathrm{ML}}(\mathbf{u})) = K < \min\{M, N\}$, $\mathbf{T}_{\mathrm{ML}}(\mathbf{u})$ admits the Vandermonde decomposition:

$$\mathbf{T}_{\mathrm{ML}}(\mathbf{u}) = \sum_{k=1}^{K} p_k\, \mathbf{a}(\theta_k, r_k)\mathbf{a}^{\mathrm{H}}(\theta_k, r_k),\ p_k > 0, \tag{20}$$

$\mathbf{a}(\theta_k, r_k) = \mathbf{f}(\theta_k) \otimes \mathbf{c}_{\mathrm{t}}(r_k)$ serves as the atom of the signal model in Eq. (12), which constitutes the fundamental building block of the quantized measurements $\mathbf{X}'_{\mathcal{Q}} = \mathbf{P}\mathcal{Q}\{\mathbf{X}\}$, where $\mathbf{X} = [\mathbf{x}_1, \ldots, \mathbf{x}_L]$ and $\mathbf{X}'_{\mathcal{Q}} = [\mathbf{x}'_{\mathcal{Q},1}, \ldots, \mathbf{x}'_{\mathcal{Q},L}]$. Collecting all possible atoms yields the infinite atomic set

$$\mathcal{A} \triangleq \left\{\mathbf{a}(\theta, r)\boldsymbol{\kappa}^{\mathrm{T}} : \mathbf{a}(\theta, r) \in \mathbb{C}^{MN'}, \boldsymbol{\kappa} \in \mathbb{C}^{L}, \left\| \boldsymbol{\kappa} \right\|_2 = 1\right\}. \tag{16}$$

Based on $\mathcal{A}$, the atomic norm of $\mathbf{X}$ is[16]

$$\begin{aligned} \left\| \mathbf{X} \right\|_{\mathcal{A}} &= \inf_{\mathbf{a}(\theta_k, r_k)\boldsymbol{\kappa}_k^{\mathrm{T}} \in \mathcal{A}, \rho_k \in \mathbb{R}^+} \left\{\sum_k \rho_k : \mathbf{X} = \sum_{k=1}^{K} \rho_k\, \mathbf{a}(\theta_k, r_k)\boldsymbol{\kappa}_k^{\mathrm{T}}\right\} \\ &= \min_{\mathbf{X}, \mathbf{u}, \mathbf{W}} \mathrm{tr}(\mathbf{T}_{\mathrm{ML}}(\mathbf{u})) + \mathrm{tr}(\mathbf{W}), \\ \text{s.t. } &\begin{bmatrix} \mathbf{T}_{\mathrm{ML}}(\mathbf{u}) & \mathbf{X} \\ \mathbf{X}^{\mathrm{H}} & \mathbf{W} \end{bmatrix} \succeq 0, \end{aligned} \tag{17}$$

where $\theta_k \in (-\pi/2, \pi/2)$ and $r_k \in (0, 2\Delta f / c)$. Here, $\mathbf{W} \in \mathbb{C}^{L \times L}$ and $\mathbf{X} \in \mathbb{C}^{MN \times L}$ are optimization variables. The matrix

$$\mathbf{T}_{\mathrm{ML}}(\mathbf{u}) = \sum_{\mathbf{n}} \boldsymbol{\Theta}_{\mathbf{n}} u_{\mathbf{n}} \in \mathbb{C}^{MN' \times MN'} \tag{18}$$

is a Toeplitz-block-Toeplitz matrix parameterized by $\mathbf{u} \in \mathbb{C}^{N_{\mathbf{u}}}$ with $N_{\mathbf{u}} = 2MN' - M - N' + 1$[10]. Here, $u_{\mathbf{n}}$ denotes the element of $\mathbf{u}$ indexed by $\mathbf{n} = [n_1, n_2]^{\mathrm{T}} \in \mathbb{N}_{\mathbf{u}}$, whose explicit structure is given in Eq. (19). Moreover, $\boldsymbol{\Theta}_{\mathbf{n}} = \boldsymbol{\Theta}_{n_2} \otimes \boldsymbol{\Theta}_{n_1}$, where $\boldsymbol{\Theta}_{n_2}$ and $\boldsymbol{\Theta}_{n_1}$ are elementary Toeplitz matrices with ones on the corresponding n_1th or n_2th diagonals and zeros elsewhere. The specific structure of the optimization variable $\mathbf{u}$ is

from which the parameter estimates $(\hat{\theta}_k, \hat{r}_k)$ $(k = 1, \ldots, K)$ can be directly retrieved.

Since $\mathbf{X}$ is composed of only a few atoms from $\mathcal{A}$, it is intrinsically sparse in the continuous atomic domain. Consequently, estimating (θ_k, r_k) can be formulated as an ANM-based sparse recovery problem. Different from conventional ANM, the measurements are subject to 1-bit quantization, which motivates the following sign-constrained 1-bit-2D-ANM formulation:

$$\begin{aligned}&\min_{\mathbf{X}} \left\| \mathbf{X} \right\|_{\mathcal{A}},\\ &\text{s.t. } \Re(\mathbf{X}'_{\mathcal{Q}}) \odot \Re(\mathbf{P}\mathcal{Q}\{\mathbf{X}\}) \geqslant 0,\\ &\quad \Im(\mathbf{X}'_{\mathcal{Q}}) \odot \Im(\mathbf{P}\mathcal{Q}\{\mathbf{X}\}) \geqslant 0,\end{aligned} \tag{21}$$

where the inequalities $\geqslant$ are applied element-wise.

3.2 The 1-bit-2D-FIPM for 1-bit-2D-ANM

To solve Eq. (21) efficiently, we rewrite it via convex relaxation as the following conic optimization problem:

$$\begin{aligned}&\min_{\mu} f(\mu) = \eta\left[\mathrm{tr}(\mathbf{T}_{\mathrm{ML}}(\mathbf{u})) + \mathrm{tr}(\mathbf{W})\right] + \left\| -\mathrm{sign}(\mathbf{y}_{\mathrm{vec}} \odot \mathbf{x}_{\mathrm{vec}}) \right\|_1,\\ &\text{s.t. } \mu \in \mathcal{K} \triangleq \left\{ (\mathbf{u}, \mathbf{X}, \mathbf{W})_{\mathrm{tuple}} : \mu = \begin{bmatrix} \mathbf{T}_{\mathrm{ML}}(\mathbf{u}) & \mathbf{X} \\ \mathbf{X}^{\mathrm{H}} & \mathbf{W} \end{bmatrix} \succeq 0 \right\},\end{aligned} \tag{22}$$

where $\mu = (\mathbf{u}, \mathbf{X}, \mathbf{W})_{\mathrm{tuple}}$ denotes the ordered tuple of optimization variables $\mathbf{u}, \mathbf{X}, \mathbf{W}$. The vectors

$$\mathbf{x}_{\mathrm{vec}} = \left[\mathrm{vec}(\Re(\mathbf{PX}))^{\mathrm{T}}, \mathrm{vec}(\Im(\mathbf{PX}))^{\mathrm{T}} \right]^{\mathrm{T}} \in \mathbb{C}^{2MNL}$$

and

$$\mathbf{y}_{\mathrm{vec}} = \left[\mathrm{vec}\left(\Re(\mathbf{X}'_{\mathcal{Q}})\right)^{\mathrm{T}}, \mathrm{vec}\left(\Im(\mathbf{X}'_{\mathcal{Q}})\right)^{\mathrm{T}} \right]^{\mathrm{T}} \in \mathbb{C}^{2MNL}$$

collect the real and imaginary parts of the compressed signal and the corresponding 1-bit quantized observations, respectively.

The term $\left\| -\mathrm{sign}(\mathbf{y}_{\mathrm{SQ}} \odot \mathbf{x}_{\mathrm{SQ}}) \right\|_1$ counts the number of sign mismatches between the recovered signal $\mathbf{X}$ (after compression by $\mathbf{P}$) and the 1-bit quantized measurements $\mathbf{X}'_{\mathcal{Q}}$. The parameter η is a regularization weight that balances sign consistency and sparsity promotion, which is usually obtained empirically. In this paper, $\eta = \sqrt{(L + \ln MN + \sqrt{2L\ln MN})\sigma}$ refers to the parameter setting in Ref. [17].

3.2.1 Barrier function for the constraints

To solve Eq. (22) using a numerical iterative scheme, we regularize the objective function by introducing a barrier term. The barrier function $F(\mu)$ is typically chosen as a logarithmic function defined over the interior of the feasible set $\mathcal{K}$. Specifically, for $\mu \in \mathrm{int}\mathcal{K}$, where $\mathrm{int}\mathcal{K}$ denotes the interior of $\mathcal{K}$, the barrier function is

$$\begin{aligned}F(\mu) &= -\ln\det\begin{bmatrix} \mathbf{T}_{\mathrm{ML}}(\mathbf{u}) & \mathbf{X} \\ \mathbf{X}^{\mathrm{H}} & \mathbf{W} \end{bmatrix}\\ &= -\ln\det\left(\mathbf{T}_{\mathrm{ML}}(\mathbf{u})\right) - \ln\det\left(\mathbf{W} - \mathbf{X}^{\mathrm{H}}\mathbf{T}_{\mathrm{ML}}^{-1}(\mathbf{u})\mathbf{X}\right).\end{aligned} \tag{23}$$

This barrier function enables the algorithm to approach the optimal solution from the interior of the feasible region[18]. It guarantees strict feasibility at every iteration, since $F(\mu)$ tends to infinity as μ approaches the boundary of $\mathcal{K}$.

By incorporating $F(\mu)$ into the original objective $f(\mu)$, the constrained problem is transformed into an unconstrained one, which is amenable to gradient-based optimization. The resulting barrier-augmented problem is

$$\min_{\mu}\left(f(\mu) + t^{-1}F(\mu)\right), \tag{24}$$

where $t > 0$ is the barrier parameter. As t increases during the iterations, the term $t^{-1}F(\mu)$ increasingly enforces the constraint $\mu \in \mathcal{K}$, and the solution of Eq. (24) converges to that of the original semidefinite programming (SDP) in Eq. (17).

3.2.2 Update of the central path

Let $\mu^{(t_i)} = (\mathbf{u}^{(t_i)}, \mathbf{X}^{(t_i)}, \mathbf{W}^{(t_i)})_{\mathrm{tuple}}$ denote the solution of Eq. (24) at the ith iteration with $t = t_i$. The augmented Karush-Kuhn-Tucker (KKT) conditions associated with Eq. (24) are

$$\begin{cases} \nabla_{\mu}\mathcal{L}\left(\mu^{(t_i)}\Lambda^{(t_i)}\right) = 0,\\ \Lambda^{(t_i)} = -t_i^{-1}\nabla F\left(\mu^{(t_i)}\right),\ \Lambda^{(t_i)} = \left(\mathbf{z}^{(t_i)}\mathbf{S}^{(t_i)}\mathbf{V}^{(t_i)}\right)_{\mathrm{tuple}},\\ \mu^{(t_i)} \in \mathcal{K},\\ \Lambda^{(t_i)} \in \mathcal{K}^* \triangleq \{\Lambda : \mu\Lambda \geqslant 0,\ \forall \mu \in \mathcal{K}\}, \end{cases} \tag{25}$$

where $\mathcal{L}(\mu, \Lambda) = f(\mu) - \langle \mu, \Lambda \rangle$ denotes the Lagrangian function, $\langle \mu, \Lambda \rangle$ corresponds to the real inner product. The dual variable Λ denotes the ordered triple tuple of dual optimization variables, which is

$$\Lambda \triangleq (\mathbf{z}, \mathbf{S}, \mathbf{V})_{\mathrm{tuple}}, \tag{26}$$

and the inner product between the primal and dual variables is

$$\left\langle \mu, \Lambda \right\rangle = \mathrm{tr}\left(\mathbf{V}^{\mathrm{H}}\mathbf{W}\right) + \Re\left\{\mathrm{tr}\left(\mathbf{S}^{\mathrm{H}}\mathbf{X}\right)\right\} + \mathbf{z}^{\mathrm{T}}\mathbf{u}, \tag{27}$$

following the standard definition in Ref. [18]. Here, $\mathcal{K}^*$ denotes the dual cone associated with $\mathcal{K}$ and specifies the feasible set of the dual variables.

At each iteration, the points $\{(\mu^{t_i}, \Lambda^{t_i}), t_i > 0\}$ satisfy the augmented KKT conditions in Eq. (25) and lie on the central path[18]. As t_i increases, the pair $(\mu^{(t_i)}, \Lambda^{(t_i)})$ progressively approaches the optimal solution of Eq. (22).

We define the gradient of a real-valued scalar function $f_{\mathbb{R}}(\mu) \in \mathbb{R}$ with respect to all optimization variables as the tuple of partial derivatives

$$\nabla f_{\mathbb{R}} = \left(\frac{\partial f_{\mathbb{R}}}{\partial \mathbf{u}}, \frac{\partial f_{\mathbb{R}}}{\partial \mathbf{X}}, \frac{\partial f_{\mathbb{R}}}{\partial \mathbf{W}} \right)_{\mathrm{tuple}}, \tag{28}$$

where $\partial f_{\mathbb{R}}/\partial \mathbf{u} \in \mathbb{C}^{N_{\mathbf{u}}}$, $\partial f_{\mathbb{R}}/\partial \mathbf{X} \in \mathbb{C}^{MN\times L}$, and $\partial f_{\mathbb{R}}/\partial \mathbf{W} \in \mathbb{C}^{L\times L}$ are computed separately, and the overall gradient $\nabla f_{\mathbb{R}}$ is defined as the collection of these components. Additionally, the gradient with respect to the complex vector $\mathbf{x} = \mathbf{a} + \mathrm{j}\mathbf{b}$ is understood as $\partial f/\partial \mathbf{x} = (\partial f/\partial \mathbf{a} - \mathrm{j}\partial f/\partial \mathbf{b})/2$[19].

By applying the Eqs. (25) and (28), the dual feasible solution is

$$\begin{aligned}\Lambda^{(t_i)} &= \nabla f\left(\mu^{(t_i)}\right) = \left(\mathbf{z}^{(t_i)}, \mathbf{S}^{(t_i)}, \mathbf{V}^{(t_i)}\right)_{\text{tuple}} \\ &= \left(\eta \frac{\partial \mathrm{tr}(\mathbf{T}_{\mathrm{ML}}(\mathbf{u}))}{\partial \mathbf{u}}\bigg|_{\mathbf{u}=\mathbf{u}^{(t_i)}}, \right. \\ &\quad \left. \frac{\partial \left\| -\mathrm{sign}(\mathbf{y}_{\mathrm{vec}} \odot \mathbf{x}_{\mathrm{vec}})\right\|_1}{\partial \mathbf{X}}\bigg|_{\mathbf{X}=\mathbf{X}^{(t_i)}}, \eta\mathbf{I}\right)_{\text{tuple}}.\end{aligned} \tag{29}$$

To compute $\partial \mathrm{tr}(\mathbf{T}_{\mathrm{ML}}(\mathbf{u}))/\partial \mathbf{u}$ in Eq. (29), we introduce the adjoint operator $\mathbf{toep}^*: \mathbb{C}^{MN\times MN} \to \mathbb{C}^{N_{\mathbf{u}}}$[20,21], which satisfies the following inner product relation:

$$\langle \mathbf{toep}^*(\mathbf{Q}), \mathbf{u}\rangle = \langle \mathbf{Q}, \mathbf{T}_{\mathrm{ML}}(\mathbf{u})\rangle, \tag{30}$$

for any Hermitian matrix $\mathbf{Q} \in \mathbb{C}^{MN\times MN}$ and $\mathbf{u} \in \mathbb{C}^{N_{\mathbf{u}}}$.

Based on the representation of $\mathbf{T}_{\mathrm{ML}}(\mathbf{u})$ as a linear combination of elementary Toeplitz matrices $\mathbf{\Theta}_{\mathbf{n}}$ (Eq. (18)), the inner product in Eq. (30) can be expressed as

$$\begin{aligned}\left\langle \mathbf{Q}, \mathbf{T}_{\mathrm{ML}}(\mathbf{u})\right\rangle &= \mathrm{tr}(\mathbf{Q}^{\mathrm{H}}\mathbf{T}_{\mathrm{ML}}(\mathbf{u})) = \mathrm{tr}\left(\left(\mathbf{T}_{\mathrm{ML}}(\mathbf{u})\right)^{\mathrm{H}}\mathbf{Q}\right) \\ &= \mathrm{tr}\left(\mathbf{T}_{\mathrm{ML}}(\mathbf{u})\mathbf{Q}\right) = \sum_{\mathbf{n}} \mathrm{tr}\{u_{\mathbf{n}}\mathbf{\Theta}_{\mathbf{n}}\mathbf{Q}\} \\ &= \sum_{\mathbf{n}} q_{\mathbf{n}}u_{\mathbf{n}} = \mathbf{q}^{\mathrm{T}}\mathbf{u} = \left\langle \mathbf{q}, \mathbf{u}\right\rangle,\end{aligned} \tag{31}$$

where the nth element of $\mathbf{q}$ is given by $q_{\mathbf{n}} = \mathrm{tr}\{\mathbf{\Theta}_{\mathbf{n}}\mathbf{Q}\}$, and according to the definition in Eq. (30), $\mathbf{toep}^*(\mathbf{Q}) = \mathbf{q}$. Thus, the adjoint operator $\mathbf{toep}^*: \mathbb{C}^{MN\times MN} \to \mathbb{C}^{N_{\mathbf{u}}}$ acting on any Hermitian matrix $\mathbf{Q} \in \mathbb{C}^{MN\times MN}$ is defined as $\mathbf{q} = \mathbf{toep}^*(\mathbf{Q})$, where the nth element of $\mathbf{q}$ is

$$q_{\mathbf{n}} = \mathrm{tr}\left\{\mathbf{Q}\frac{\partial \mathbf{T}_{\mathrm{ML}}(\mathbf{u})}{\partial u_{\mathbf{n}}}\right\} = \mathrm{tr}\{\mathbf{\Theta}_{\mathbf{n}}\mathbf{Q}\}, \quad \mathbf{n} \in \mathbb{N}_{\mathbf{u}}.$$

Moreover, from linearity of the derivative and trace, the following equality holds

$$\mathbf{q} = \mathbf{toep}^*(\mathbf{Q}) = \frac{\partial}{\partial \mathbf{u}}\left\langle \mathbf{q}, \mathbf{u}\right\rangle = \frac{\partial}{\partial \mathbf{u}}\mathrm{tr}\left(\mathbf{Q}^{\mathrm{H}}\mathbf{T}_{\mathrm{ML}}(\mathbf{u})\right). \tag{32}$$

Now, let $\mathbf{Q} = \mathbf{I}$, then

$$\frac{\partial}{\partial \mathbf{u}}\mathrm{tr}(\mathbf{T}_{\mathrm{ML}}(\mathbf{u})) = \mathbf{toep}^*(\mathbf{I}) \triangleq \mathbf{\xi}. \tag{33}$$

For $\partial\left\|-\mathrm{sign}(\mathbf{y}_{\mathrm{vec}} \odot \mathbf{x}_{\mathrm{vec}})\right\|_1 / \partial \mathbf{X}\big|_{\mathbf{X}=\mathbf{X}^{(t_i)}}$, following Ref. [22], the gradient of the sign-mismatch function $f_{\mathrm{flip}}(x) = \left\|-\mathrm{sign}(y \odot x)\right\|_1 \in \mathbb{R}$ with $y \in \{-1, 1\}$ is

$$\frac{\partial f_{\mathrm{flip}}(x)}{\partial x} = \frac{1}{2}(\mathrm{sign}(x) - y), \tag{34}$$

which gives

$$\mathbf{S}^{(t_i)} = \frac{1}{2}\mathbf{P}^{\mathrm{T}}\left[\mathrm{sign}\left(\mathbf{P}\mathbf{X}^{(t_i)}\right) - \mathbf{X}'_{\mathcal{Q}}\right]. \tag{35}$$

Combining Eqs. (33) and (35) with Eq. (29), the analytical form of the dual solution $\Lambda^{(t_i)}$ is

$$\begin{cases}\mathbf{z}^{(t_i)} = \eta\mathbf{\xi}, \\ \mathbf{S}^{(t_i)} = \frac{1}{2}\mathbf{P}^{\mathrm{T}}\left[\mathrm{sign}\left(\mathbf{P}\mathbf{X}^{(t_i)}\right) - \mathbf{X}'_{\mathcal{Q}}\right], \\ \mathbf{V}^{(t_i)} = \eta\mathbf{I}.\end{cases} \tag{36}$$

Substituting Eq. (36) into the second equation (complementarity condition) of Eq. (25) yields the primal solution $\mu^{(t_i)}$:

$$\begin{aligned}&\mathbf{X}^{(t_i)} \approx \mathbf{T}_{\mathrm{ML}}\left(\mathbf{u}^{(t_i)}\right)\mathbf{P}^{\mathrm{T}}\left(\mathbf{T}_{\mathrm{ML}}\left(\mathbf{u}^{(t_i)} + 4\eta\mathbf{e}_0\right)\mathbf{P}^{\mathrm{T}}\right)^{-1}\mathbf{X}'_{\mathcal{Q}}, \\ &\mathbf{W}^{(t_i)} = (\eta t_i\mathbf{I})^{-1} + \mathbf{X}^{(t_i)\mathrm{H}}\left(\mathbf{T}_{\mathrm{ML}}\left(\mathbf{u}^{(t_i)}\right)\right)^{-1}\mathbf{X}^{(t_i)},\end{aligned} \tag{37}$$

where the approximation $\mathrm{sign}(\mathbf{X}^{(t_i)}) \approx \mathbf{X}^{(t_i)}$ is used in solving for $\mathbf{X}^{(t_i)}$, and $\mathbf{u}^{(t_i)}$ is the solution to

$$\eta\mathbf{\xi} - \eta\mathbf{toep}^*\left(\mathbf{\Phi}\mathbf{\Phi}^{\mathrm{H}}\right) - t_i^{-1}\mathbf{toep}^*\left[(\mathbf{T}_{\mathrm{ML}}(\mathbf{u}))^{-1}\right] = 0, \tag{38}$$

with the unit vector $\mathbf{e}_0 \in \mathbb{R}^{N_{\mathbf{u}}}$, whose first element is one and all others are zero, and $\mathbf{\Phi} = \mathbf{P}^{\mathrm{T}}\left[\mathbf{P}\mathbf{T}_{\mathrm{ML}}(\mathbf{u} + 4\eta\mathbf{e}_0)\mathbf{P}^{\mathrm{T}}\right]^{-1}\mathbf{X}'_{\mathcal{Q}}$. Except for $\mathbf{u}^{(t_i)}$, for which only an implicit solution is available, all other primal-dual variables in Eqs. (37) and (38) have explicit forms.

To solve Eq. (38) for $\mathbf{u}^{(t_i)}$, we define an optimization problem about $\mathbf{u}$:

$$h(\mathbf{u}) = \eta\mathbf{\xi}^{\mathrm{T}}\mathbf{u} + \eta\,\mathrm{tr}\left\{\mathbf{X}'^{\mathrm{H}}_{\mathcal{Q}}\left[\mathbf{P}\mathbf{T}_{\mathrm{ML}}(\mathbf{u} + 4\eta\mathbf{e}_0)\mathbf{P}^{\mathrm{T}}\right]^{-1}\mathbf{X}'_{\mathcal{Q}}\right\}$$

and

$$H(\mathbf{u}) = -\ln\det(\mathbf{T}_{\mathrm{ML}}(\mathbf{u})).$$

Then, setting the gradient of $\psi(\mathbf{u}) = h(\mathbf{u}) + t_i^{-1}H(\mathbf{u})$ to zero is equivalent to solving Eq. (38). Consequently, the point satisfying $\nabla_{\mathbf{u}}\psi(\mathbf{u}) = 0$ is the optimal solution of the following unconstrained convex problem:

$$\min_{\mathbf{u}} \psi(\mathbf{u}) = h(\mathbf{u}) + t_i^{-1}H(\mathbf{u}). \tag{39}$$

Thus, solving the polynomial Eq. (38) is approximately equivalent to solving Eq. (39), which can be efficiently tackled using quasi-Newton method[21] or Newton method[18]. The optimal solution $\mathbf{u}$ for Eq. (39) is used to update $\mathbf{u}^{(t_i)}$.

Clearly, the numerically approximated primal-dual central path $\{(\mu^{(t_i)},\Lambda^{(t_i)}),t_i>0\}$ derived from Eqs. (36) and (37) satisfies the first two conditions of Eq. (25). Regarding the third condition, it is also evident that the update steps in each iteration ensure that $\mathbf{T}_{\mathrm{ML}}(\mathbf{u}^{(t_i)})\succ 0$. Moreover, under the conditions $\eta>0$ and $t_i>0$, the solution for $\mathbf{W}^{(t_i)}$ in Eq. (37) ensures that

$$\mathbf{W}^{(t_i)}-\mathbf{X}^{(t_i)\mathrm{H}}\left(\mathbf{T}_{\mathrm{ML}}\left(\mathbf{u}^{(t_i)}\right)\right)^{-1}\mathbf{X}^{(t_i)}=(\eta t_i\mathbf{I})^{-1}\succ 0, \tag{40}$$

holds true at each iteration. By the Schur complement lemma, we conclude that $\mu^{(t_i)}\in\operatorname{int}\mathcal{K}$, and hence the third condition in Eq. (25) is also satisfied.

3.2.3 The barrier parameter update and the implementation of 1-bit-2D-FIPM

As to the variations due to the iterations, increasing the barrier parameter t forces a decrease of the dual gap, meaning that the dual feasible solution and the primal feasible solution converge to the same optimal solution of Eq. (22). To this end, we discuss the method for updating the barrier parameter.

According to Eq. (25), the primal variable at $\mu=\mu^\star$ satisfies $\nabla\mathcal{L}(\mu^\star,\Lambda)=0$, which leads to the Lagrangian function $\mathcal{L}(\mu,\Lambda)$ reaching its lower bound for all $\mu\in\mathcal{K}$. The dual function g at the dual point $\Lambda=-t^{-1}\nabla F(\mu^\star)=-t^{-1}(\mu^\star)^{-1}$ is

$$\begin{aligned}g(\Lambda)&=\inf_{\mu\in\mathcal{K}}\mathcal{L}(\mu,\Lambda)\\&=\mathcal{L}(\mu^\star,\Lambda)\\&=f(\mu^\star)-t^{-1}\mathrm{tr}\left\{\mu^\star\left(\mu^\star\right)^{-1}\right\}\\&=f(\mu^\star)-t^{-1}\left(MN'+L\right),\end{aligned} \tag{41}$$

where the ideal dual gap $\eta^\star=f(\mu^\star)-g(\Lambda)=t^{-1}\left(MN'+L\right)$. Thus, for any $\mu\in\mathcal{K}$, the dual gap η satisfies

$$\eta=f(\mu)-g(\Lambda)\geqslant\eta^\star=t^{-1}\left(MN'+L\right). \tag{42}$$

By computing the dual function $g(\Lambda)$ at each iteration, we substitute Eq. (36) into the dual function $g(\Lambda^{(t_i)})=\inf_{\mu\in\mathcal{K}}\mathcal{L}(\mu,\Lambda^{(t_i)})$, which can be derived as

$$\begin{aligned}g\left(\Lambda^{(t_i)}\right)=&\left\|-\mathrm{sign}\left(\mathbf{y}_{\mathrm{vec}}\odot\mathrm{vec}\left(\mathbf{P}\mathbf{X}^{(t_i)}\right)\right)\right\|_1\\&-\mathrm{tr}\left\{\frac{1}{2}\mathbf{X}^{(t_i)\mathrm{H}}\mathbf{P}^{\mathrm{T}}\left[\mathrm{sign}\left(\mathbf{\Gamma}\mathbf{X}^{(t_i)}\right)-\mathbf{X}'_{\mathcal{Q}}\right]\right\}.\end{aligned} \tag{43}$$

By recalling the reference lower bound function $f_{\mathrm{LB}}=\max\{f_{\mathrm{LB}},g(\Lambda^{(t_i)})\}$, we can update the barrier parameter t for the next iteration as

$$t_{i+1}=\gamma\frac{MN'+L}{f\left(\mu^{(t_i)}\right)-f_{\mathrm{LB}}}, \tag{44}$$

where $\gamma>1$ is preselected to control the update step size.

The 1-bit-2D-FIPM developed in this paper returns an acceptable solution when the duality gap at the ith iteration ($i>0$), corresponding to the solution $(\mu_i,\Lambda_i)=(\mu^{(t_i)},\Lambda^{(t_i)})$, satisfies $\eta_i=f(\mu^{(t_i)})-f_{\mathrm{LB}}\leqslant\epsilon_{\mathrm{gap}}$, where ϵ_{gap} is set as the stop threshold. The algorithm continuously smooths the hard threshold of the SDP constraints and approximates the optimal point via the central path. In summary, the proposed method is presented in Algorithm 1.

Algorithm 1 1-bit gridless CS-based target positioning algorithm for accurate underwater localization

Parameters: barrier parameter update step size $\gamma>1$, regularization parameter η, convergence threshold ϵ_{gap}

Input: Received signal $\mathbf{X}'_{\mathcal{Q}}$

Output: Range-anlge parameters $(\hat{\theta}_k,\hat{r}_k)$, for $k=1,\ldots,K$

1. Initialize $i=0$, $f_{\mathrm{LB}}=-\infty$, and μ_0,Λ_0 using Eqs. (36) and (37), where $\mathbf{u}_0=\left(\frac{\left\|\mathbf{X}'_{\mathcal{Q}}\right\|_{\mathrm{F}}^2}{MN},0,\ldots,0\right)^{\mathrm{T}}$
2. **while** $\eta_i\geqslant\epsilon_{\mathrm{gap}}$ **do**
3. $i=i+1$
4. Update $\mathbf{u}^{(t_i)}$ by solving Eq. (39) using the L-BFGS algorithm
5. Calculate $g(\Lambda^{(t_i)})$ using Eq. (43), and update $f_{\mathrm{LB}}=\max\{f_{\mathrm{LB}},g(\Lambda^{(t_i)})\}$
6. Update the barrier parameter t_{i+1} using Eq. (44)
7. **end while**
8. Retrieve the range-anlge parameters frequencies $(\hat{\theta}_k,\hat{r}_k)$, for $k=1,\ldots,K$, from $\mathbf{T}_{\mathrm{ML}}(\hat{\mathbf{u}})$ using the Vandermonde decomposition in Eq. (20)

4 Complexity analysis

The computational efficiency of the proposed algorithm also depends on the complexity of each iteration, which can be analyzed in terms of the number of flops. Specifically, traditional general-purpose convex optimization toolboxes (e.g., sdpt3, sedumi, and other Matlab Software for Disciplined Convex Programming toolboxes) require the construction of an SDP problem of dimension $(MN'+L)^2$ when solving Eq. (22), leading to a worst-case complexity of $\mathcal{O}[(MN'+L)^6]$[21,23]. However, the primal-dual variable solution forms in Eqs. (36) and (37) significantly reduce the number of optimization variables that need to be handled.

Additionally, the most computationally expensive operation in Algorithm 1 is the inversion of the Toeplitz-block-

Toeplitz matrices, which dominates the overall complexity of the algorithm. We recommend using the 2D Levinson-Durbin method[24] for fast Toeplitz-block-Toeplitz matrix inversion. This method blocks the Toeplitz-block-Toeplitz matrices and computes the solution iteratively, which can be performed efficiently with $\mathcal{O}\left[N'^3(M^2-M+2)\right]$ flops.

5 Simulation results

In the experiments, although the transmitted signal at each sensor has a bandwidth of 5 Hz, the overall FDA-MIMO signal bandwidth is formed by the superposition of frequency increments and amounts to 40 Hz, which is much smaller than the carrier frequency of 5 kHz. Therefore, the narrowband assumption is satisfied. The number of receiving array elements is set to 15, and the inter-element spacing of both the transmitting and receiving arrays is half a wavelength, i.e., 0.15 m. The number of signal snapshots is 16. The above parameter settings of the FDA-MIMO sonar system are summarized in Table 1.

The parameters for the proposed 1-bit-2D-FIPM are set as follows: the barrier parameter multiplier $\gamma = 5$, while both the absolute convergence threshold ϵ_{gap} are set to 10^{-4}.

In the experiments, we first generate the target echo signals received at the array. For each Monte Carlo trial, real underwater noise randomly selected from lake experiments conducted at Qiandao Lake is added to each sensor channel to evaluate the adaptability of the proposed algorithm for gridless estimation in underwater target detection. The noise data were collected using two side-looking arrays, each consisting of 16 elements, mounted on a moving platform at a water depth of approximately 30 m. Different signal-to-noise ratio (SNR) conditions are simulated by controlling the energy of the synthetically generated targets. Specifically, the SNR at the qth entry of the array ($q = 0, \ldots, MN-1$) is

$$R_{\text{SN}_q} = 10\log_{10}\left(\frac{\mathbb{E}\left[|x_{q,l}|^2\right]}{\mathbb{E}\left[|e_q|^2\right]}\right),$$

Table 1 Parameters setting

Parameter	Value
Speed of sound propagating underwater (c)	1500 m/s
Carrier frequency (f_c)	5 kHz
Bandwidth of each sensor	5 Hz
Frequency increment of FDA (Δf)	5 Hz
Element spacing of transmitting array (d_t)	0.15 m
Element spacing of receiving array (d_r)	0.15 m
Number of transmitting array elements (M)	8
Number of receiving array elements (N)	15
Number of signal snapshots (L)	16

where $x_{q,l}$ denotes the qth entry of the target component vector $\mathbf{x}'_l$, $l = 1, \ldots, L$, and e_q represents the noise component at the qth entry. We consider the noise to be equally distributed across all entries, i.e., $R_{\text{SN}} = R_{\text{SN}_q}$.

Two performance metrics are considered: the runtime, which reflects the computational efficiency, and the root-mean-square error (RMSE) of the angle and range estimates, defined as

$$\text{RMSE}_\theta = \sqrt{\frac{1}{2KN_{\text{MC}}}\sum_{n=1}^{N_{\text{MC}}}\sum_{k=1}^{K}\left(\widehat{\theta}_{k,n}-\theta_k\right)^2},$$

$$\text{RMSE}_r = \sqrt{\frac{1}{2KN_{\text{MC}}}\sum_{n=1}^{N_{\text{MC}}}\sum_{k=1}^{K}\left(\hat{r}_{k,n}-r_k\right)^2},$$

where N_{MC} denotes the number of Monte Carlo trials, $\widehat{\theta}_{k,n}$ and $\hat{r}_{k,n}$ represent the estimated angle and range of the kth target in the nth trial, respectively, whereas θ_k and r_k are the corresponding ground-truth values.

5.1 Sensitivity analysis of the selection of η

In this section, we investigate the sensitivity of the proposed 1-bit-2D-FIPM algorithm to different settings of the parameter η. The sonar-related system parameters are set according to Table 1. The value of η computed from $\eta = \sqrt{(L+\ln MN+\sqrt{2L\ln MN})\sigma}$ is taken as the nominal reference, and offset values ranging from -10 to 10 are added to generate the actual η used in the experiments.

For each parameter setting, 100 Monte Carlo trials are conducted. In each trial, five targets are randomly generated, and joint range-angle estimation is performed. The RMSEs of range and angle, as well as the computational time, are recorded under different η settings. Figure 2 illustrates the impact of different η values on the range and angle estimation RMSEs of the proposed algorithm.

The results show that when η is set in the vicinity of the value given by $\eta = \sqrt{(L+\ln MN+\sqrt{2L\ln MN})\sigma}$, specifically for offset values in the range of -4–2, the proposed 1-bit-2D-FIPM algorithm achieves low RMSEs for both range and angle estimation, together with fast convergence, as reflected by shorter computational time. These observations indicate that the proposed algorithm exhibits a certain degree of robustness with respect to the parameter η, allowing moderate deviations from the theoretically derived setting without significant performance degradation.

5.2 Performance comparison for multi-target detection

In this subsection, the proposed 1-bit-2D-FIPM is

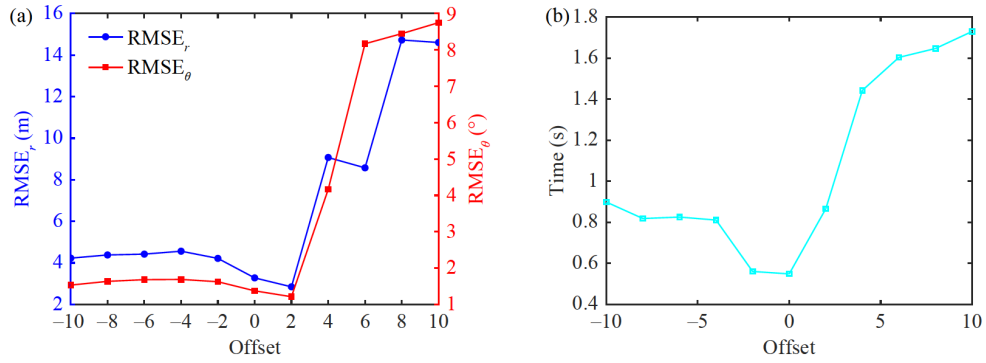


Fig. 2 RMSE and runtime versus different offset values of η: (a) RMSE; (b) Runtime.

compared with ANM-based accelerate proximal gradient (ANM-APG)[2] and 2D-ESPRIT[4] for joint range-angle estimation in multi-target detection using an FDA-MIMO sonar system.

The FDA-MIMO sonar parameters adopted in the simulations are summarized in Table 1. All experiments are conducted in a noisy environment with an SNR of −5 dB. To comprehensively evaluate the resolving capability of the algorithms, several representative target configurations are considered, including:

(1) Targets A and B, which share the same range;

(2) Targets B and C, which share the same angle;

(3) Targets D and E, which are closely spaced in both range and angle.

The corresponding range and angle settings of these targets are provided in Table 2.

Figure 3 shows the results of 100 Monte Carlo trials used to evaluate the sparsity-promoting denoising performance of ANM-APG, 2D-ESPRIT, and the proposed 1-bit-2D-FIPM. The true target locations are indicated by black circles, while the estimated range-angle pairs obtained by each method are marked by blue plus signs.

The poor estimation accuracy of 2D-ESPRIT mainly stems from the holes introduced by virtual array expansion, which distort the covariance matrix structure and consequently degrade the underlying signal subspace. As a result, the estimates produced by 2D-ESPRIT exhibit large deviations from the true target positions. In contrast, gridless CS methods do not rely on a complete covariance matrix. Instead, parameter recovery is achieved by exploiting sparse representations over a continuous atomic set together with Toeplitz-structured constraints, which provides much stronger robustness to virtual array holes. This fundamental difference explains why the proposed method consistently outperforms 2D-ESPRIT in virtual array scenarios.

Table 2 Positions of the targets

	A	B	C	D	E
Range (m)	112.8	112.8	83.8	24.8	35.2
Angle (°)	16.3	33.6	16.3	55.6	62.2

For ANM-APG, when only 1-bit quantized measurements are available, the use of inappropriate fitting constraints leads to wrong estimates in target configurations with identical angles but different ranges, or identical ranges but different angles. In particular, false targets appear in some Monte Carlo trials, such as a non-existent target at (33.6°, 83.8 m).

In contrast, the proposed 1-bit-2D-FIPM successfully resolves these challenging scenarios, accurately discriminating between targets A, B, and C, as well as between targets D and E that are closely spaced in both range and angle.

Table 3 reports the angle RMSE, range RMSE, the final iteration number I_{final} for ANM-APG and 1-bit-2D-FIPM, as well as the computational time of the three algorithms over 100 Monte Carlo trials. Consistent with the results shown in Fig. 3, the proposed 1-bit-2D-FIPM achieves the smallest RMSE$_\theta$ and RMSE$_r$. Moreover, by explicitly exploiting the quantization-aware constraints, 1-bit-2D-FIPM converges in fewer iterations than ANM-APG, which in turn leads to a noticeably reduced computational time.

In summary, the proposed 1-bit-2D-FIPM, realized via efficient numerical iterations and appropriately designed quantization-aware constraints, is capable of accurately recovering the underlying sparse signal from 1-bit quantized data associated with a virtual array containing missing elements induced by array expansion. As a result, it enables reliable estimation of the key target parameters with fewer iterations and reduced computational time. Owing to its superior performance, the proposed algorithm provides an effective solution for accurate target positioning in active FDA-MIMO sonar systems based on 1-bit gridless CS.

5.3 Performance under different numbers of elements of receiving array

In this section, experiments are conducted to compare the performance of different algorithms under varying numbers of receiving array elements. The number of receiving array elements ranges from 9 to 25 with an increment

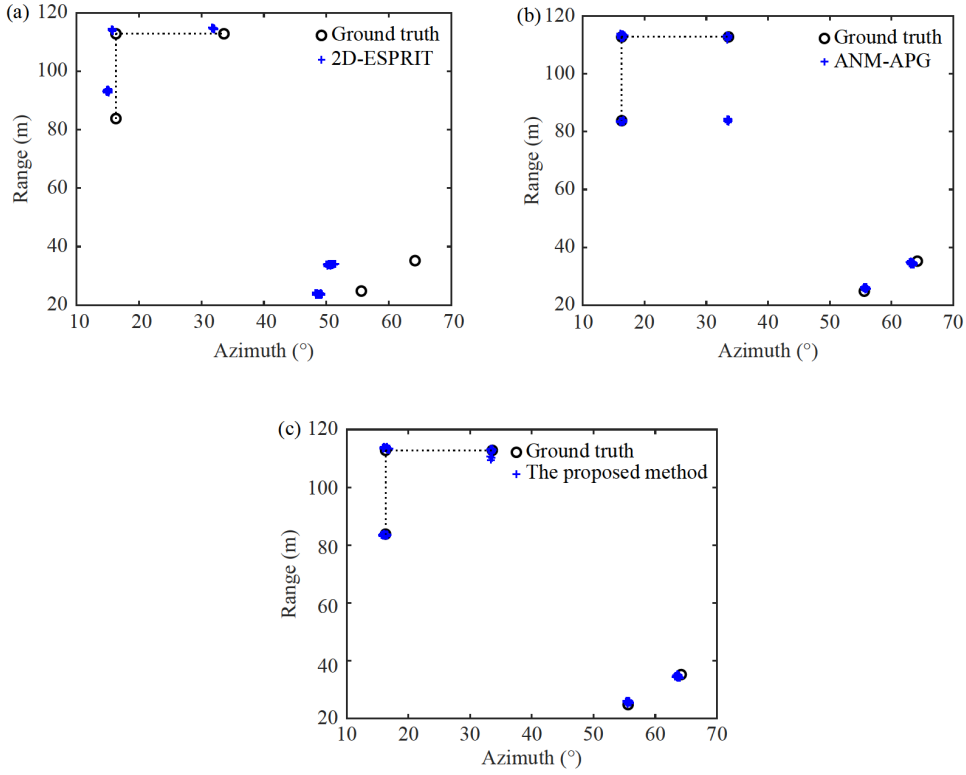


Fig. 3 Range-angle joint estimation results for multiple targets using different algorithms: (a) 2D-ESPRIT; (b) ANM-APG; (c) 1-bit-2D-FIPM.

Table 3 Summary of algorithm performance

	2D-ESPRIT	ANM-APG	The proposed method
RMSE_θ (°)	6.8457	8.1670	0.3509
RMSE_r (m)	4.8433	1.6833	0.6877
I_{final}	–	34	16
Runtime (s)	0.0024	1.1436	0.5488

of 2. Five targets are randomly generated, while all other experimental parameters follow those listed in Table 1. The SNR is set to −5 dB. The proposed 1-bit-2D-ANM method is compared with ANM-APG[2], 2D-ESPRIT[4], DANM[13], and 1-bit-RANM[14]. The corresponding results are shown in Fig. 4. As the number of receiving array elements increases, all considered algorithms exhibit a decreasing trend in RMSE for both range and angle estimation. In particular, the proposed 1-bit-2D-ANM method and the 1-bit-RANM method consistently achieve the lowest estimation errors across all array sizes. In contrast, ANM-APG, 2D-ESPRIT, and DANM suffer from noticeably larger estimation errors, as they do not incorporate quantization-aware constraints.

Figure 5 depicts the computational time required by different methods. Owing to its decoupling strategy, the DANM method reduces the problem dimensionality and therefore achieves relatively low computational complexity,

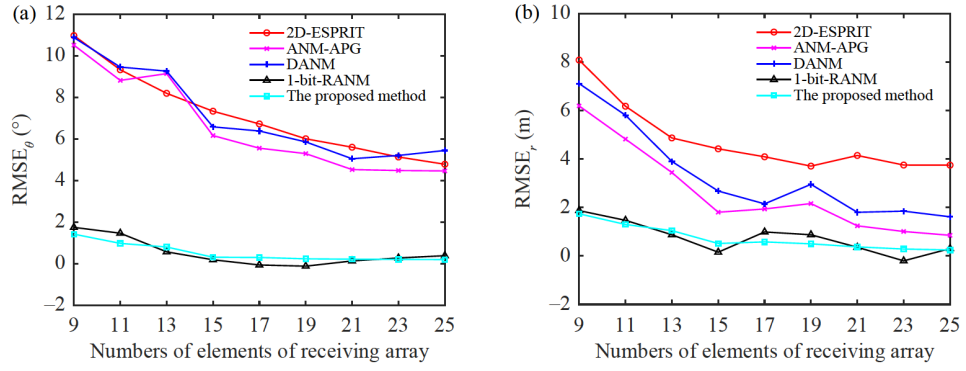


Fig. 4 RMSEs versus different numbers of elements of receiving array: (a) RMSE_θ; (b) RMSE_r.

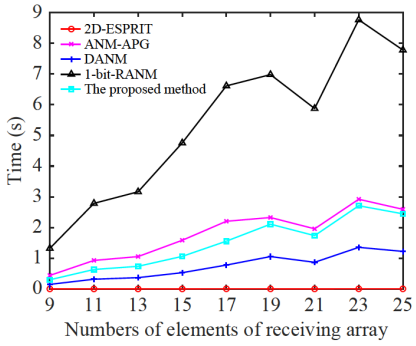


Fig. 5 Runtimes versus different numbers of elements of receiving array.

while 2D-ESPRIT is the fastest since it does not involve iterative optimization. In addition, the proposed 1-bit-2D-ANM method attains a favorable trade-off between estimation accuracy and computational cost. It maintains low RMSE with an acceptable runtime, and its computational time remains nearly unchanged as the receiving array size increases, consistently staying below 2 s.

5.4 Performance under different SNR

Subsequently, we evaluate the performance of the proposed algorithm under different SNR levels. Five targets are randomly selected, while the remaining experimental parameters follow those listed in Table 1. The SNR varies from −15 dB to 15 dB with a step size of 5 dB. As shown in Fig. 6, the proposed 1-bit-2D-FIPM exhibits robust performance, achieving consistently lower RMSE_{θ} and RMSE_{r} over the entire SNR range compared with the other methods. These results demonstrate the effectiveness and reliability of the proposed approach under varying noise conditions.

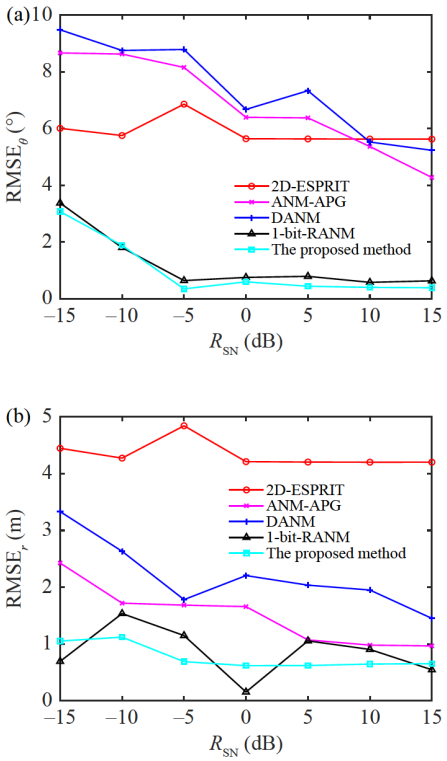


Fig. 6 RMSEs versus different SNR levels: (a) RMSE_{θ}; (b) RMSE_{r}.

6 Conclusion

This paper proposes a 1-bit gridless joint range-angle estimation framework for FDA-MIMO sonar systems, aiming at accurate target localization on resource-limited underwater platforms. By introducing a virtual array expansion strategy, the inherent range-angle coupling is explicitly decoupled while enlarging the effective aperture. To address the resulting missing virtual elements and severe quantization constraints, a 1-bit atomic norm minimization-based gridless CS formulation is developed and efficiently solved via 1-bit-2D-FIPM, achieving low storage requirements, reduced computational complexity, and high estimation accuracy. Simulation results using real underwater noise demonstrate that the proposed method consistently outperforms existing approaches in terms of accuracy, robustness, and runtime, particularly in low-SNR and multi-target scenarios. Nevertheless, the proposed framework relies on an idealized 1-bit quantization model and focuses on static scenarios, while non-ideal receiver effects and target dynamics are not explicitly considered. Future work will therefore investigate more realistic sensing models, including multi-bit or adaptive quantization, as well as extensions to dynamic scenarios and more computationally efficient implementations for real-time FDA-MIMO sonar systems.

References

[1] Wu M, Hao C, Hu Q, *et al*. Sparsity-based processing to enhance the reverberation suppression for FDA-MIMO sonars. *IEEE Trans. Aerosp. Electron. Syst.*, 2023, **60**(2): 1556–1569

[2] Tang W G, Jiang H, Zhang Q. Range-angle decoupling and estimation for FDA-MIMO radar via atomic norm minimization and accelerated proximal gradient. *IEEE Signal Process. Lett.*, 2020, **27**: 366–370

[3] Xiong J, Wang W Q, Gao K. FDA-MIMO radar range–angle estimation: CRLB, MSE, and resolution analysis. *IEEE Trans. Aerosp. Electron. Syst.*, 2017, **54**(1): 284–294

[4] Yan Y, Cai J, Wang W Q. Two-stage ESPRIT for unambiguous angle and range estimation in FDA-MIMO radar. *Digit. Signal Process.*, 2019, **92**: 151–165

[5] Walden R H. Analog-to-digital converter survey and analysis. *IEEE J. Sel. Areas Commun.*, 2002, **17**(4): 539–550

[6] Mao X, Pan H. An improved DOA estimation algorithm based on wavelet operator. *J. Commun.*, 2013, **8**(12): 839–844

[7] Huang X, Liao B. One-bit MUSIC. *IEEE Signal Process. Lett.*, 2019, **26**(7): 961–965

[8] Ruan N, Wang H, Wen F, *et al*. DOA estimation in B5G/6G: trends and challenges. *Sensors*, 2022, **22**(14): 5125

[9] Donoho D L. Compressed sensing. *IEEE Trans. Inf. Theory*, 2006, **52**(4): 1289–1306

[10] Yang Z, Xie L, Stoica P. Vandermonde decomposition of multilevel Toeplitz matrices with application to multidimensional super-resolution. *IEEE Trans. Inf. Theory*, 2016, **62**(6): 3685–3701

[11] Chi Y, Chen Y. Compressive two-dimensional harmonic retrieval via atomic norm minimization. *IEEE Trans. Signal Process*., 2014, **63**(4): 1030–1042

[12] Li S, Yang D, Tang G, *et al*. Atomic norm minimization for modal analysis from random and compressed samples. *IEEE Trans. Signal Process*., 2018, **66**(7): 1817–1831

[13] Gao Y, Wu M, Hao C, *et al*. Efficient gridless range-angle estimation for active sonar systems based on 2D fast interior-point method. *IEEE Trans. Aerosp. Electron. Syst*., 2025, **61**(5): 13123–13136

[14] Li R, Yang J, Dai Z, *et al*. High-resolution and robust one-bit direction-of-arrival estimation via reweighted atomic norm estimation. *Sensors*, 2024, **24**(18): 14

[15] Chen Y, Chi Y. Spectral compressed sensing via structured matrix completion. *J. Mach. Learn. Res*., 2013, **28**(3): 414–422

[16] Yang Y, Chu Z, Ping G. Two-dimensional multiple-snapshot grid-free compressive beamforming. *Mech. Syst. Signal Process*., 2019, **124**: 524–540

[17] Yang Z, Li J, Stoica P, *et al*. Sparse methods for direction-of-arrival estimation. In: Chellappa R, Theodoridis S (eds). Academic press library in signal processing, volume 7. London: Academic Press, 2018: 509–581

[18] Boyd S P, Vandenberghe L. Convex optimization. Cambridge: Cambridge University Press, 2004

[19] van Trees H L. Detection, estimation, and modulation theory: optimum array processing. New York: Wiley, 2001

[20] Dumitrescu B. Positive trigonometric polynomials and signal processing applications. Berlin: Springer, 2007

[21] Hansen T L, Jensen T L. A fast interior-point method for atomic norm soft thresholding. *Signal Process*., 2019, **165**: 7–19

[22] Tang W G, Jiang H, Zhang Q. One-bit gridless DOA estimation with multiple measurements exploiting accelerated proximal gradient algorithm. *Circuits Syst. Signal Process*., 2022, **41**(2): 1100–1114

[23] Sidiropoulos N D, Davidson T N, Luo Z Q. Transmit beamforming for physical-layer multicasting. *IEEE Trans. Signal Process*., 2006, **54**(6): 2239–2251

[24] Dai F, Wang Y, Hong L. Gohberg-Semencul factorization-based fast implementation of sparse bayesian learning with a Fourier dictionary. *IEEE Trans. Geosci. Remote Sens*., 2022, **60**: 1–15